THIS IS AN EARLY ACCESS ARTICLE.
This article has been accepted for publication in a future issue of this journal,
but has not been fully edited. Content may change prior to final publication.

BULLETIN OF THE POLISH ACADEMY OF SCIENCES
TECHNICAL SCIENCES
DOI: 10.24425/bpasts.2027.7726

Multibody modelling and verification of a Lightweight Unmanned Ground Vehicle

D. Tomica[*1], L. Śnieżek[1], A. Rubiec[1], T. Muszyński[1], P. Krogul, D[1]. Szpaczyńska[1]

[1] Faculty of Mechanical Engineering, Military University of Technology, Kaliskiego 2, 00 - 908 Warsaw, Poland

Abstract. Unmanned Ground Vehicles (UGVs) are widely used in hazardous and unpredictable environments. Their drive and undercarriage systems are subjected to complex dynamic loads that can affect operational reliability. Simulation models can be used to analyse these forces, but existing studies often rely on simplified models that neglect some of important factors. The aim of this study is to develop, parameterize and numerically verify a detailed multibody model of a lightweight tracked UGV, with particular emphasis on the representation of the track system, suspension, drivetrain components and contact interactions. The verified model is intended to provide a basis for subsequent experimental validation and detailed load analysis. The model was created by using CAD-based geometry of a real platform and contained detailed representations of track segments, suspension elements, drivetrain components, and their interactions. The results demonstrate that the model reproduces key aspects of a real system and after validation can be used for further load analysis.

Key words: Unmanned Ground Vehicle (UGV), multibody dynamics, model building, load analysis, tracked vehicle modelling component,

1. INTRODUCTION

Unmanned ground vehicles (UGVs), particularly lightweight mobile robotic platforms, are increasingly used in applications requiring reliable operation in challenging and unstructured environments [1–6]. They enable remote or autonomous execution of tasks in locations that are difficult to access or hazardous to human operators, including inspection, monitoring, and technical intervention [4, 7–9].

Lightweight mobile robots have demonstrated high effectiveness in a wide range of applications involving operation in hazardous or restricted environments [10], [11][12–14]. The increasing availability of synthetic chemical substances has raised concerns related to accidental or unauthorised handling of dangerous materials in civilian contexts [15]. As a result, incidents involving hazardous objects or materials may pose significant risks to public safety in densely populated or infrastructurally complex areas [16, 17]. In many such cases, risk mitigation and neutralisation tasks are carried out by specialised response teams equipped with protective equipment and lightweight mobile robotic platforms, which enhance operational safety and efficiency by enabling remote intervention and reducing direct human exposure [18–20].

The construction of lightweight mobile robots, combining compact dimensions with high obstacle-negotiation capability, allows them to operate in a wide range of demanding terrain conditions. A critical feature of these robots is their ability to operate, for example, in urban areas, on soft ground, through water obstacles, or in mountainous terrain [10, 11, 21, 22]. Many of these robots use tracked drive systems, which reduce ground pressure and facilitate motion on low-bearing-capacity surfaces such as mud or snow. However, their undercarriage and drive systems are subjected to various dynamic loads, including vertical loads caused by terrain irregularities, lateral loads associated with abrupt changes in direction, and fatigue loads during prolonged operation [23, 24].

The operational cycle of mobile robots typically comprises three stages: reaching the mission site, performing the assigned task (including motion with a load held by the manipulator), and returning to the home base. The drive and undercarriage systems are used during each of these stages. Therefore, their efficiency and reliability are critical to mission success. Failure of either system may compromise the mission, underscoring the importance of robust design and reliable assessment of drivetrain and undercarriage loads [25].

Current research trends [28-39] focus primarily on three areas: the development of mapping and navigation software [26–29], the design of new robotic systems [30–33] and simulation of drive and undercarriage loads [34–37]. A broad overview of mathematical approaches used to describe the kinematics and dynamics of wheeled and tracked UGVs is provided in [38] including formulations accounting for longitudinal and lateral forces, turning resistance and vehicle–terrain interaction. However, multibody models provide the possibility of explicitly representing individual components, constraints and contact interactions. This paper focuses on the third area. In this field, several modelling approaches can be distinguished, differing primarily in the degree of model simplification. One of the most important simplifications concerns the representation of the tracks. One approach reduces track-system

This article has been accepted for publication in a future issue of this journal, but has not been fully edited. Content may change prior to final publication.

complexity by increasing the diameter of the support wheels while omitting the track itself. This representation, referred to as a string track model, significantly reduces the number of degrees of freedom and, consequently, the computational cost. However, its accuracy may be limited, particularly when simulating motion over hard surfaces with small irregularities. In the same model, the geometry of individual drivetrain components was also simplified by replacing them with basic solids [39].

Another modelling approach uses a multibody track representation, which is more complex than the previously described method but still does not necessarily reproduce the actual geometry of all components. Such models account not only for the connections between wheels and track segments but also for interactions between the track system and suspension components. Including these interactions is important because it enables a more realistic representation of impacts, friction, and motion resistance arising from contact between multiple bodies [40–42]. One commonly used formulation is impact contact, implemented in software such as MSC Adams and its ATV (Adams Tracked Vehicle) module [39]. ATV provides a ready-made environment for modelling tracked vehicles and enables rapid model development without constructing the tracks from first principles. A more comprehensive application of the Adams Tracked Vehicle toolkit was presented by Grazioso et al. [43].who developed and experimentally validated a multibody model of a tracked robot equipped with a passive articulated suspension. Particular attention was paid to the representation of the suspension swing arms and the rubber track belt. The validated model was subsequently used to assess the suspension performance under different operating configurations. However, its predefined structure limits detailed parameter adjustment and the representation of selected phenomena relevant to the present modelling approach. More recently, Febbraro et al. [44] proposed a highly detailed object-oriented multibody model of a tracked agricultural robot, including a discretised flexible track, complete suspension system and track–terrain interaction. An important feature of this approach is its capability to represent both rigid and deformable terrain, with the model experimentally validated under indoor and outdoor conditions.

A dynamic model of a track system incorporating spring-damping elements was developed in [45]. However, this model did not account for the actual geometry of components such as individual track links, the drive wheel, or the road wheels. This approach primarily stems from the fact that using CAD models of the vehicle significantly increases computation time.

A more detailed approach incorporating the actual geometry of components omitted in the previously described study was proposed in [46]. In this model, the components are characterised by parameters such as mass and moments of inertia. However, the geometry of selected components, including suspension arms, torsion beams, and drive wheels, was simplified to reduce computational complexity. Retaining detailed geometry is particularly important for components such as wheels and track links because these directly govern local contact interactions. Consequently, such models can provide a more faithful representation of the physical system.

Similar research was reported in [7]. In that study, contact constraints were defined between 32 track elements, connected by rotational joints, and the drive wheel. Spring-damper elements were included, and track tension was represented using a spring-damper component positioned between the support wheels and the drive wheel. The study also emphasised the role of the suspension system in absorbing impact loads and distributing forces between the track and the ground. However, friction between the track links, drive wheel, and support slides was neglected, while the obstacles were represented as rigid, non-deformable bodies [7]. Multibody simulation has also been applied specifically to the assessment of obstacle-negotiation capabilities of lightweight tracked UGVs. Szpaczyńska et al. [47] compared several multi-tracked running-gear configurations using obstacle-crossing simulations and experimentally identified terrain parameters, demonstrating the usefulness of MBD models for evaluating mobility-related performance at the vehicle level.

Although simplifications can reduce model-development and simulation time, they may also reduce model fidelity. Therefore, an appropriate balance between computational efficiency and physical representation must be established. Existing studies predominantly focus on track modelling, while fewer works comprehensively integrate track dynamics, suspension behaviour, drivetrain mechanisms, and inter-component contact interactions. The primary objective of this study is therefore to develop, parameterise, and numerically verify a detailed multibody model of a lightweight tracked UGV. The verification focuses on track-belt behaviour, contact interactions, suspension representation, numerical stability, time-step sensitivity, and model response to changes in vehicle velocity. The resulting model is intended as a basis for subsequent experimental validation and further analysis of drivetrain and undercarriage loads.

2. UNMANNED GROUND VEHICLE MODELLING

The modelling process was conducted in a multibody simulation environment using MSC Adams/View. The model was based on a real mobile platform used in engineering and intervention operations (Figure 1). The modelling procedure was intended to reproduce the dynamics of the drive and undercarriage systems, with particular emphasis on the interactions governing load transmission during operation.

Before developing the simulation model, described in Sections 2.2–2.4, a structural decomposition of the UGV was carried out (Section 2.1). This enabled the identification of the subsystems and components most relevant to mechanical load transmission, while less significant elements, such as mission-specific accessories, were simplified or omitted. The modelling procedure began with the development of accurate 3D geometry, which served as the basis for the subsequent multibody simulation and numerical verification.

*e-mail: dawid.tomica@wat.edu.pl

This article has been accepted for publication in a future issue of this journal, but has not been fully edited. Content may change prior to final publication.



Fig.1. Modeled Unmanned Ground Vehicle [48].

2.1. UGV decomposition.

The modelled UGV is a lightweight tracked platform designed for patrol and intervention tasks [48]. Its main structure comprises a central body (red), interchangeable mission modules such as a manipulator, sensor packages, or neutralisation tools (blue), a track belt (black), and the drive and undercarriage system (green) (Figure 2).

In the configuration used for modelling, external mission-specific elements such as X-ray modules or hazardous-material handling tools were omitted because of their variability and relatively small influence on drivetrain dynamics.

In the configuration used for modelling, external mission-specific elements such as the x-ray modules or hazardous material handling tools were omitted due to their variability and relatively low impact on the drivetrain dynamics.

The subsequent sections focus on the essential mechanical subsystems of the robot. The components most relevant to the present model are the undercarriage, drivetrain, and track-belt systems (Figure 3), including:

- the drive wheel - transmitting torque from the electric motors to the track;
- road wheels - five pairs per track, connected through spring-damping suspension units;
- idler wheel - responsible for track tension adjustment;
- support slides (rollers) - reducing track sag and maintaining belt alignment;

an elastomer track belt - constructed from reinforced rubber segments.

All these elements are integrated within the tracked running gear. Their interactions determine the dynamic response of the robot, particularly during motion over irregular terrain and obstacle negotiation. Track pretension was introduced through the front idler-wheel tensioning mechanism. The idler wheel

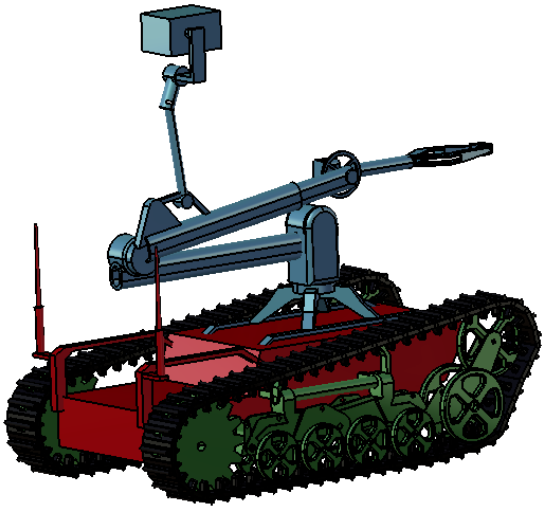


Fig.2. UGV decomposition effect: blue - manipulator, red - body, black - track belt, green - undercarriage.

to the connected to the chassis through a spring-damper element. The initial position/deflection of this element defined the initial track pretension, while its compliance allowed the tension to vary dynamically during vehicle motion.

Following the structural decomposition, detailed geometric models of the retained assemblies were created and imported into the simulation software. These CAD models formed the basis of the multibody model and enabled the calculation of internal forces, moments, and relative displacements within the undercarriage system.

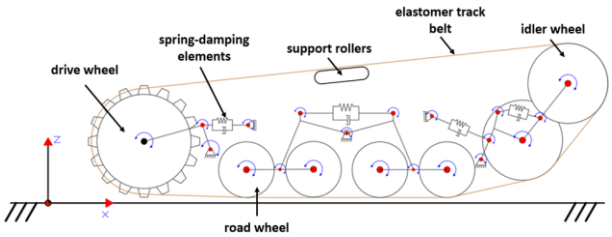


Fig.3. UGV undercarriage, drive and track belt systems.

2.2. UGV mass properties.

To support reliable dynamic analysis, a detailed 3D geometric model of the UGV was developed from direct measurements of the physical platform. The components were reconstructed in CATIA V5 and exported in STEP format for import into the MSC Adams/View.

- The geometric model includes: the central chassis structure, treated as a rigid body;
- five pairs of double road wheels per track;
- suspension arms and torsion beams;
- front idler wheels with spring-loaded tensioners;
- drive wheels with realistic tooth geometry;
- a 54-segment discretized discretised track belt model;
- the manipulator treated as a single rigid body.

This article has been accepted for publication in a future issue of this journal, but has not been fully edited. Content may change prior to final publication.

To minimise computational cost while preserving mechanical realism, minor geometric simplifications were applied to the arms and supporting structures. However, the geometry of the track teeth, road wheels, and drive wheels was retained in detail because these components govern local contact interactions and force transmission. The mass and inertia properties of each component were determined from the assigned material density and corresponding geometric model. The calculated values are summarised in Table 1 and identified in Figure 4.

TABLE 1. Mass and inertia properties of the UGV model components

No.	I_{xx}, kgmm^2	I_{yy}, kgmm^2	I_{zz}, kgmm^2	Number of elements	m_i, kg	Total weight, kg
1.	3639	1843	1843	2	6.89	13.78
2.	718	622	153	2	0.37	0.73
3.	160	82	82	16	0.10	1.57
4.	48885	44066	6347	2	3.22	6.43
5.	356	278	77	8	0.15	1.17
6.	145	136	11	8	0.07	0.52
7.	704	643	61	4	0.21	0.85
8.	781	395	395	6	0.21	1.25
9.	165	125	40	2	0.14	0.29
10.	63	63	12	108	0.07	7.88
11.	6313	4676	1902	1	7.25	7.25
12.	423	408	23	1	49.75	49.75
				SUM	160	91,47

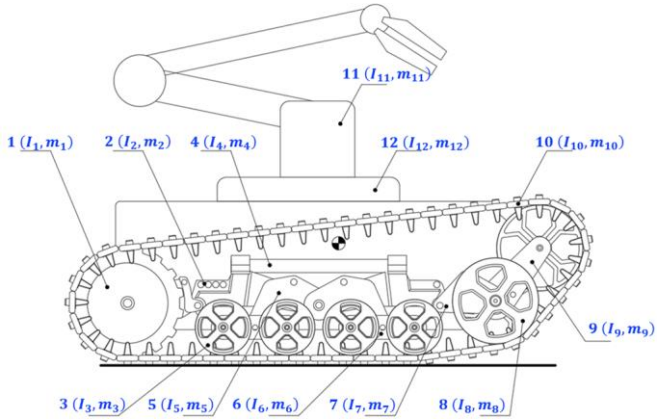


Fig.4. Main UGV model components and their mass and inertia properties.

2.3. Track belt model.

The modelled UGV uses an elastomeric track belt. The track consists of an elastomer belt reinforced with longitudinally oriented aramid cords that carry tensile loads. Additional drive and guide teeth ensure proper engagement with the drive wheel and guide the track along the road wheels and supporting elements. The outer surface of the track is equipped with tread blocks that improve ground contact, traction, and mobility on uneven terrain (Figure 5).

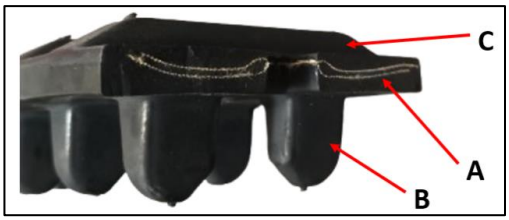


Fig.5. Structure of the UGV track belt: A - main reinforcing cords (transmitting tensile forces in the track), B - drive-guide teeth, C - tread block

To replicate the real behaviour of the track while adequately simplifying its model, a CAD model was first created by dividing the track belt into 54 identical segments (Figure 6). A force-based connection was introduced between adjacent segments, allowing angular and translational displacements in selected directions.

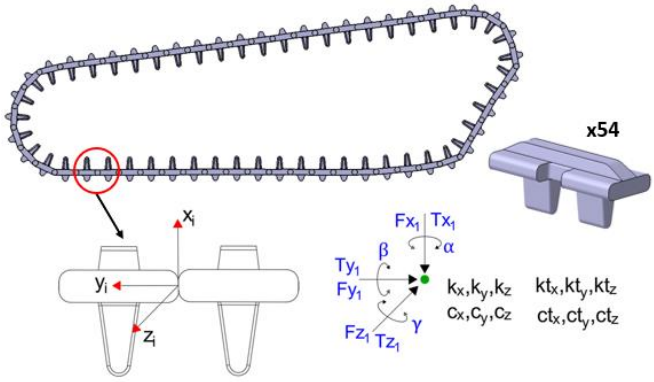


Fig.6. Track belt model.

The forces and moments between the segments are calculated using a stiffness-damping matrix, where the user-defined values are the stiffness and damping coefficients:

$$\begin{bmatrix} F_x \\ F_y \\ F_z \\ T_x \\ T_y \\ T_z \end{bmatrix} = \begin{bmatrix} k_x & 0 & 0 & 0 & 0 & 0 \\ 0 & k_y & 0 & 0 & 0 & 0 \\ 0 & 0 & k_z & 0 & 0 & 0 \\ 0 & 0 & 0 & k_{tx} & 0 & 0 \\ 0 & 0 & 0 & 0 & k_{ty} & 0 \\ 0 & 0 & 0 & 0 & 0 & k_{tz} \end{bmatrix} \cdot \begin{bmatrix} x \\ y \\ z \\ \alpha \\ \beta \\ \gamma \end{bmatrix} + \begin{bmatrix} c_x & 0 & 0 & 0 & 0 & 0 \\ 0 & c_y & 0 & 0 & 0 & 0 \\ 0 & 0 & c_z & 0 & 0 & 0 \\ 0 & 0 & 0 & c_{tx} & 0 & 0 \\ 0 & 0 & 0 & 0 & c_{ty} & 0 \\ 0 & 0 & 0 & 0 & 0 & c_{tz} \end{bmatrix} \cdot \begin{bmatrix} \dot{x} \\ \dot{y} \\ \dot{z} \\ \dot{\alpha} \\ \dot{\beta} \\ \dot{\gamma} \end{bmatrix} \quad (1)$$

where: x, y, z - linear displacements; α, β, γ - angular displacements; $k_{x,y,z}$ - linear stiffness coefficients; $k_{Tx,y,z}$ - rotational stiffness coefficients; $c_{x,y,z}$ - linear damping coefficients; $c_{Tx,y,z}$ - rotational damping, coefficients $\dot{x}, \dot{y}, \dot{z}$ - linear velocity, $\dot{\alpha}, \dot{\beta}, \dot{\gamma}$ - angular velocity.

The resultant force and torque depend on relative linear and angular displacements as well as relative linear and angular velocities between the connected track segments. When no relative motion or rotation occurs between the markers, the resulting forces and torques are equal to zero.

This article has been accepted for publication in a future issue of this journal, but has not been fully edited. Content may change prior to final publication.

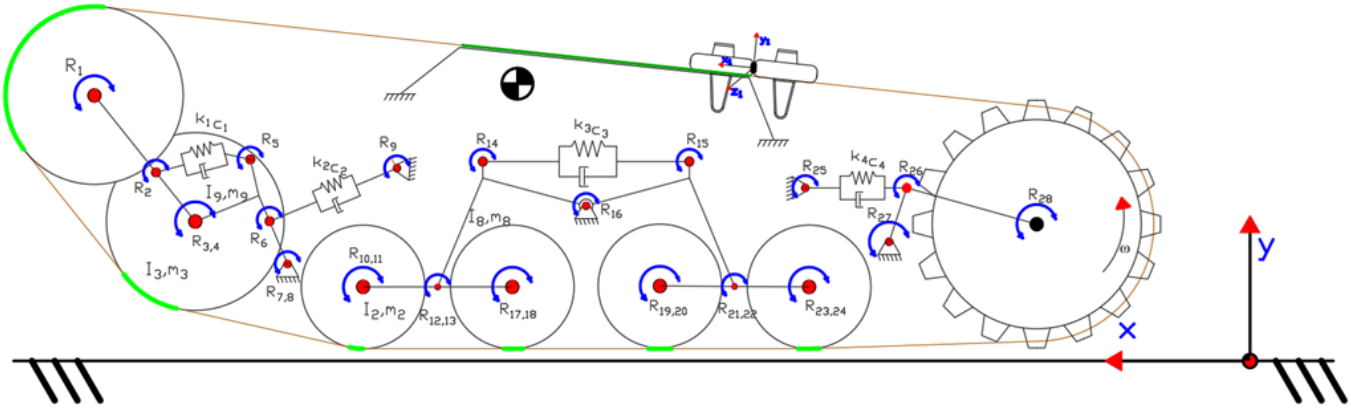


Fig.7. UGV undercarriage model structure: R - rotational joint; k - stiffness coefficient; c - damping coefficient, ω - angular velocity of drive wheel

2.4. Undercarriage model.

The undercarriage model is presented in Figure 7. All components were assumed to be rigid, and rotational joints were applied where required. The model consists of 298 rigid bodies, 78 rotational joints, and 123 fixed constraints, resulting in 710 degrees of freedom.

When preparing the model, several assumptions were introduced to maintain a balance between the representation of the relevant physical phenomena and the computational complexity of the multibody system.

All structural components of the UGV undercarriage were represented as rigid bodies. This assumption was adopted because the primary objective of the model is to reproduce the global dynamics and load transmission within the track, suspension and drivetrain systems rather than local structural deformation. Introducing flexible bodies would considerably increase the computational cost of an already complex model containing a discretised 54-segment track belt and numerous contact interactions. Consequently, local elastic deformation and stress distribution within individual structural components are outside the scope of the present model.

Clearances in the rotational joints were neglected. Explicit representation of joint clearances would require additional contact definitions and contact parameters, further increasing both the numerical complexity and computational cost. Therefore, the present model does not reproduce impact phenomena that could result from backlash or wear in individual joints.

The ground was represented as a rigid, non-deformable surface. This assumption corresponds to the current scope of the numerical verification, which considers motion on hard surfaces and obstacle negotiation. Consequently, the present model should not be directly interpreted as representing UGV operation on deformable soil. The model architecture nevertheless allows the rigid-ground formulation to be replaced by a deformable-terrain or terramechanical interaction model in subsequent studies. Such an extension would affect both motion resistance and the transmission of dynamic loads through the track-terrain interface because deformable terrain introduces additional compliance and energy dissipation that are absent for a rigid surface.

During the verification simulations, vehicle motion was prescribed by applying angular velocity directly to the rotational joints of the drive sprockets. This kinematic excitation provides a controlled and repeatable input, which is particularly useful for assessing contact stability, numerical convergence and sensitivity to vehicle velocity. The developed model is not restricted to this excitation method, and the prescribed angular velocity can be replaced by a drive torque or by a more detailed actuator model in subsequent applications.

3. UGV MODEL PARAMETRISATION AND VERIFICATION

Once the geometry and structural layout of the UGV were established, the next step in developing the simulation model was the precise definition of its physical and interaction parameters. Due to the complexity of multibody dynamics in tracked vehicles, a wide range of parameters must be defined to faithfully capture real-world behaviour. These include:

- parameters governing track segment connectivity;
- contact characteristics between rigid bodies;
- mechanical properties of spring-damper elements;
- initial conditions and driving input.

At this stage, the methodology focused on defining the initial parameter values and numerically verifying the behaviour of the developed model.

The adopted approach was intended to ensure that the model represents not only the geometry of the robot but also the internal force transmission and dynamic response of the system under the analysed conditions. The verification procedure assessed the response of the model to changes in key parameters. Successful completion of this stage provides a basis for subsequent experimental identification, validation of the complete UGV model, and detailed load analysis.

3.1. Track belt.

The stiffness and damping coefficients used in the track-belt model should ultimately be determined through a combined static and dynamic identification procedure. Following the methodology described in [49], the stiffness coefficients are first adjusted on the basis of a static test so that the calculated track deflection corresponds to that measured for the physical track belt. In the subsequent dynamic test, the stiffness is further

This article has been accepted for publication in a future issue of this journal, but has not been fully edited. Content may change prior to final publication.

refined to reproduce the oscillation period of the physical system, while the damping coefficients are adjusted to reproduce the decay of oscillations and the number of observable vibration cycles. In the present study, these experimental identification tests were not yet performed. Both tests were performed exclusively in the numerical simulation environment and constituted part of the model verification procedure; therefore, preliminary parameter values were adopted from the literature and subsequently subjected to numerical sensitivity assessment. High stiffness and damping values were assigned in the y and z directions and for rotations α and β, while the remaining parameters were varied to assess their influence on track behaviour. This approach maintained sufficient track stiffness in directions other than the principal bending direction over the wheels. Two tests were prepared (Figure 8): (a) a static test, in which the track deflection under its own weight was evaluated as a function of selected parameters; and (b) a dynamic test, in which changes in the damping behaviour were observed with respect to variations in individual parameters. Due to the nature of the test, the parameters governing the relative rotation between individual track segments-namely k_{tz} and c_{tz}-were varied.

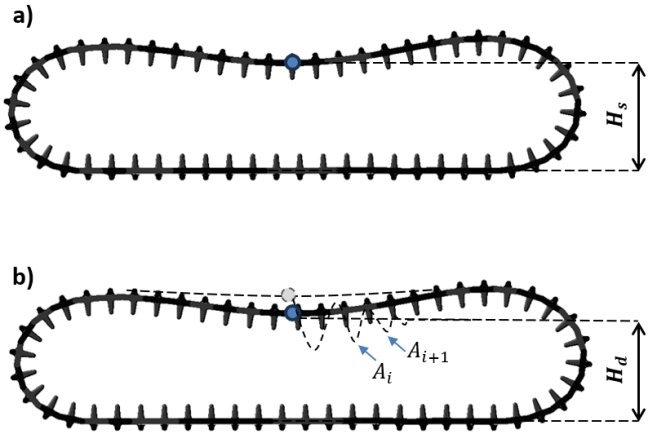


Fig.8. Schematic representation of track belt tests: (a) static; (b) dynamic; Hs - static height, Hd - dynamic height, Ai - amplitude

For the dynamic test - a 0.2 kg mass was applied to the upper surface of the track belt. The following quantities were used to evaluate the model response:

- the logarithmic decrement of damping (Figure 9), described by the following relation:

$$\delta = ln\frac{A_1}{A_2} \tag{2}$$

- the dimensionless damping ratio:

$$\xi = \frac{\delta}{\sqrt{4\pi^2+\delta^2}} \tag{3}$$

- the time constant (τ) of a second-order inertial system, defined as the time after which the amplitude decreases to A/e (Figure 9);
- the dynamic amplification factor φ defined according to the following relation:

$$\varphi_d = \frac{A_1 - e_{ust}}{e_{ust}} \tag{4}.$$

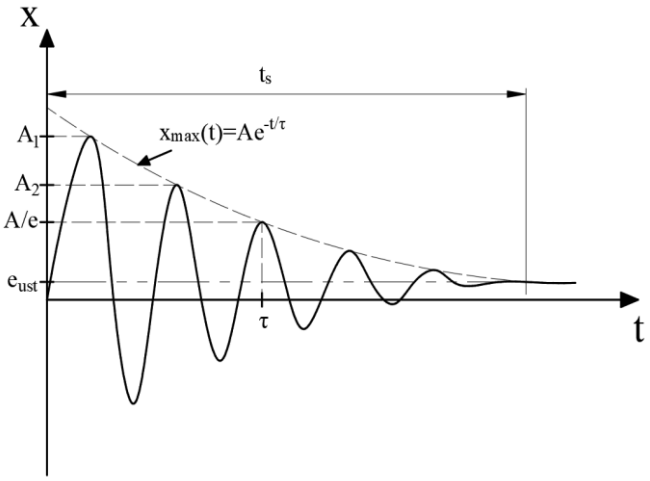


Fig.9. Typical response to a step input together with the physical interpretation of the time constant of a second-order inertial system.

TABLE 2. Results of static and dynamic verification tests of the track-belt model

No.	k_{tz}, Nmm/rad	c_{tz}, Nmms/rad	H_s, mm	δ	ξ	τ, s	φ_d
1.	6500	250	201.27	0.73	0.12	1.46	29.54
2.	6500	500	201.29	1.47	0.23	0.73	20.16
3.	6500	1000	201.37	3.14	0.45	0.34	8.2
4.	6500	150	201.37	0.44	0.07	2.42	33.95
5.	6500	350	201.36	1.03	0.16	1.04	25.39
6.	7500	250	244.43	0.64	0.10	1.46	21.33
7.	8500	250	277.42	0.60	0.10	1.33	14.88
8.	5500	250	132.58	0.81	0.13	1.79	48.39
9.	6000	250	175.23	0.76	0.12	1.59	38.28

Figure 10 presents the time histories of the track-belt height H for selected parameter configurations (1, 4, 5, 6, and 8). The response can be divided into two distinct phases. During the initial phase (0–10 s), the system undergoes free vibration and settles to a static equilibrium corresponding to track deflection under its own weight. This phase is characterised by damped oscillations whose amplitude and decay rate depend on the assumed stiffness and damping parameters

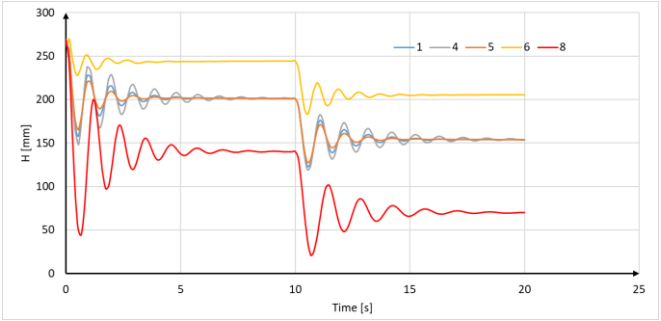


Fig.10. Time histories of track height H for selected parameter configurations under own mass and load with 0.2 kg mass.

This article has been accepted for publication in a future issue of this journal, but has not been fully edited. Content may change prior to final publication.

The parameter variation presented in Table 2 and Figure 10 constitutes a deterministic sensitivity assessment of the track model with respect to the rotational stiffness and damping. The results demonstrate that these parameters have a pronounced influence on both the static deflection and transient response of the track belt, including the oscillation decay rate, damping ratio, time constant and dynamic amplification factor. The objective of this stage was therefore not to quantify statistical parameter uncertainty, but to identify physically consistent preliminary parameter values and evaluate the responsiveness of the numerical model before experimental validation. Accordingly, the parameters listed in Table 3 should be regarded as the verified preliminary parameter set within the scope of the present study rather than as experimentally identified final values.

At $t = 10$s, an additional load is applied, resulting in a second transient response. When the additional load is applied, the system exhibits a second transient response. The track height decreases rapidly and is followed by damped oscillations until a new equilibrium position is reached. The magnitude of deflection and the dynamic response vary considerably between configurations, indicating strong sensitivity of the track model to parameter changes.

Configuration 6 exhibits the highest stiffness, with the smallest deflection and fastest stabilisation, whereas configuration 8 exhibits the largest deflection and lowest damping, resulting in more pronounced oscillations and a longer settling time. The remaining configurations (1, 4, and 5) show intermediate behaviour with similar trends but different damping characteristics.

Overall, the results confirm that the track-model response is strongly dependent on the selected stiffness and damping parameters, particularly in terms of dynamic stability and load-induced deflection. Based on the obtained characteristics and the literature, preliminary interaction-force parameters were selected from configuration 8 at this stage, bearing in mind that subsequent experimental validation was required. The values of the individual parameters defined in Eq. (1) are presented in Table 3.

TABLE 3. Values of connection parameters between track belt segments

k, N/mm		c, Ns/mm		k_t, Nmm/rad		c_t, Nmms/rad	
k_x	1e+06	c_x	1e+06	k_{tx}	1e+06	c_{tx}	1e+05
k_y	1e+03	c_y	2.5e+02	k_{ty}	1e+06	c_{ty}	1e+05
k_z	1e+06	c_z	1e+06	k_{tz}	5.5e+03	c_{tz}	2.5e+02

3.2. Contact between bodies.

Accurate representation of contact interactions between system components is essential for obtaining reliable results from multibody simulations, particularly in the case of tracked vehicles operating under complex loading conditions. In the developed UGV Contact interactions between the model components were described using the IMPACT function implemented in MSC Adams/View [50]. The IMPACT function defines the normal contact force (F) generated when the distance between the interacting bodies becomes smaller than the reference contact distance

The principle of this function can be illustrated using the collision of a sphere with a flat surface (Figure 11). When the distance between markers I and J reaches the value x1, corresponding to the onset of contact, the force generated by the IMPACT function is activated.

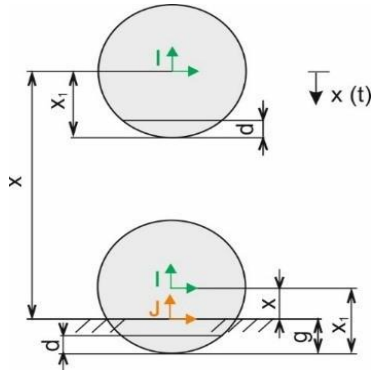


Fig.11. Function IMPACT working scheme.

As long as the distance between markers *I* and *J* is greater than x_1, this force remains equal to zero, if not it is described by the following equations [50]:

$$F = F_k + F_c \tag{6}$$

$$F = k(x_1 - x)^s - c_{max}\dot{x} \cdot STEP(x, x_1 - d, 1, x_1, 0) \tag{7}$$

where: F – contact force, F_k – stiffness component of contact force; F_c – damping component of contact force; k – contact stiffness coefficient; c – contact damping coefficient; s – contact stiffness characteristic exponent; x, x_1, d – according to Figure 11.

The stiffness component counteracts mutual penetration of the contacting surfaces (Figure 12a). The damping coefficient c, which defines the damping component of the contact force, depends on the relative penetration velocity of the two bodies. It reaches its maximum value, c_{max} at the maximum penetration depth d defined which is defined as one of the simulation parameters. (Figure 12b).

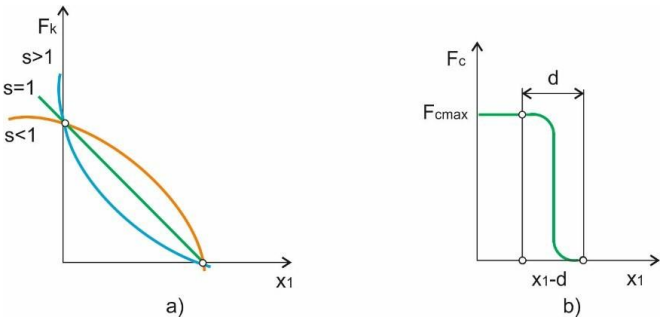


Fig.12. Characteristics of F_k (a) and F_c (b) components.

In addition to the normal contact force, tangential interactions were modelled using a Coulomb friction formulation incorporating static and dynamic friction coefficients. The transition between static and dynamic friction regimes was controlled using predefined velocity thresholds.

This article has been accepted for publication in a future issue of this journal, but has not been fully edited. Content may change prior to final publication.

Several contact pairs were defined in the model, including interactions between the track belt and the drive wheel, road wheels, supporting elements, and ground. Each pair was assigned a dedicated set of parameters, including stiffness, damping, force exponent, penetration depth, and friction coefficients. These parameters were selected to represent the physical properties of the interacting materials while maintaining stable numerical performance.

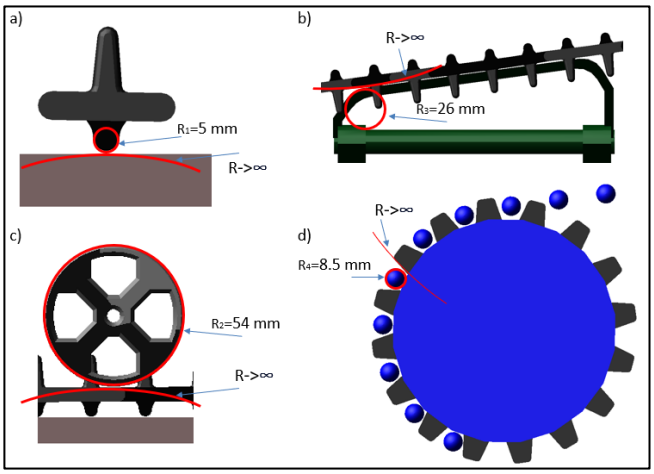


Fig.13. Contact pairs in the UGV model a) track belt - ground, b) track belt - supporting element, c) track belt - track roller, d) drive wheel - track (circumferential and radial force).

The determination of appropriate contact parameters was carried out using a comparative approach based on simulations performed in the Siemens Simcenter environment. The Simcenter contact model is based on well-defined material properties, such as Young's modulus (E), Poisson's ratio (ν), and contact geometry (sphere diameter) (Table 4), which are readily available and provide a clear physical basis for parameter definition. In contrast, the equivalent parameters used in the MSC Adams IMPACT formulation are not directly defined by conventional material properties and therefore require an additional calibration procedure. For this reason, Simcenter 3D was used as a numerical reference for the preliminary determination of the IMPACT parameters.

TABLE 4. Material datasheet for modelled elements [51]

Part name	Material	E, MPa	ν
Track belt	Elastomer	50	0.5
Drive wheel	Plastic	2500	0.4
Track roller	Plastic	2500	0.4
Supporting element	Steel	20700	0.27
Ground	Concrete	30000	0.2

Equivalent simulations were then performed in MSC Adams, where the parameters of the IMPACT function (stiffness, damping, and force exponent) were iteratively adjusted to reproduce the displacement vs. time responses obtained in Simcenter (Figure 14). The calibration process was considered satisfactory when the average relative error between the two simulation approaches was below 15%, which was deemed sufficient for the intended level of model fidelity (Figure 15). This threshold was selected as a compromise between model` accuracy and computational effort, and reflects the level of precision required at the present verification stage. Further refinement of the contact parameters was reserved for the subsequent experimental validation stage. The relative error values for the analysed contact pairs are presented in Table 5.

TABLE 5. Average relative error of sphere displacement between Adams and Simcenter simulations for different contact pairs.

Contact between track belt and:	di_w [%]
Drive wheel	11.61
Track roller	0.30
Supporting element	0.39
Ground	2.49

Based on the conducted analysis, the contact parameters assigned to individual contact pairs were set and are summarized in Table 6. Coulomb friction was also included in the model and characterised by the static friction coefficient μ_s, dynamic friction coefficient μ_d, stiction transition velocity v_s, and friction transition velocity v_d. These parameters were assigned constant values for each individual contact pair based on the material properties and characteristics of the interacting surfaces. The adopted values ensure numerical stability of the model while maintaining a physically consistent representation of contact interactions between the cooperating elements of the track system. Particular attention was paid to the proper selection of stiffness and damping coefficients, as these parameters significantly influence both the magnitude and distribution of dynamic loads within the undercarriage system.

TABLE 6. Contact parameters in the UGV model

Contact between track belt and:	k, N/mm	s	c, Ns/mm	d, mm
Drive wheel	57.0	1.460	0.0014	0.5
Track roller	69.0	1.454	0.0032	0.5
Supporting element	56.0	1.452	0.0045	0.5
Ground	58.0	1.459	0.0011	0.5
	μ_s	μ_d	v_s	v_d
Drive wheel	0.7	0.6	1	20
Track roller	0.5	0.4	1	20
Supporting element	0.6	0.5	1	20
Ground	0.7	0.6	1	20

3.3. Full UGV model.

The initial UGV model was developed to fulfil several functions required for preliminary numerical verification before experimental validation. The main objective was to assess whether the model produced physically consistent responses, remained numerically stable, and responded appropriately to variations in selected input parameters.

The first simulation scenario involved straight-line motion over a flat surface at a maximum velocity of 8 km/h, with particular emphasis on the stability of the contact interactions.

This article has been accepted for publication in a future issue of this journal, but has not been fully edited. Content may change prior to final publication.

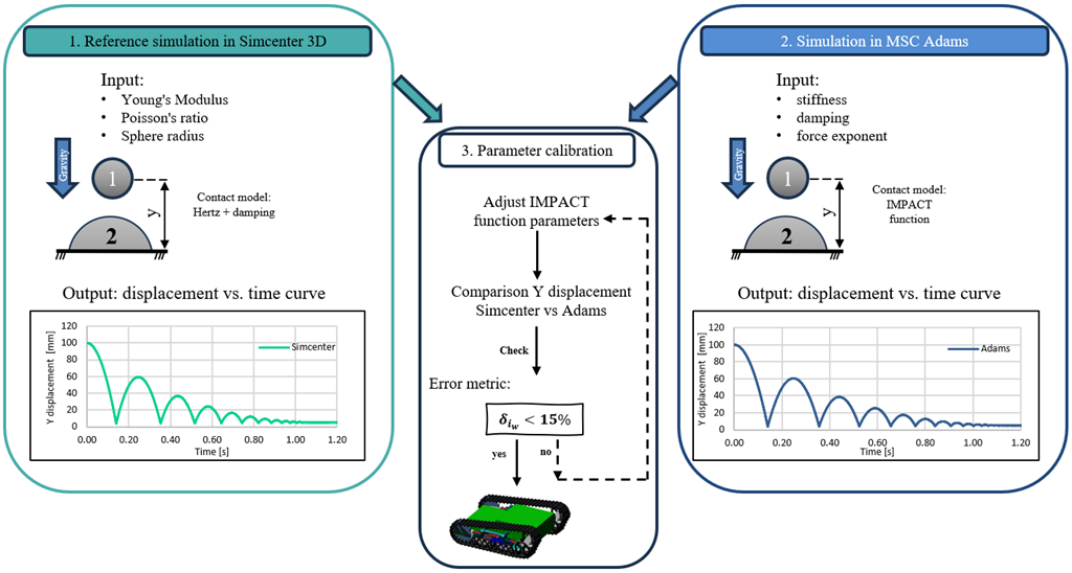


Fig.14. Calibration of sphere-sphere contact model parameters between Simcenter 3D Motion and MSC Adams.

Vehicle motion was prescribed by a STEP-defined angular velocity applied directly to both drive wheels.

The simulations were performed using the GST IFF integrator (Generalized Singly Diagonal Implicit Runge-Kutta), which is well-suited for stiff and highly nonlinear systems. Additionally, the I3 (Implicit 3) integration scheme was employed to improve numerical stability and accuracy, particularly for small time steps. A fixed time step of 0.01 s was used in the initial simulation.

During the first series of simulations, significant non-physical oscillations were observed in the contact force between the track and the ground (Figure 16). Their magnitude and frequency indicated numerical instability and made the results unsuitable for further analysis.

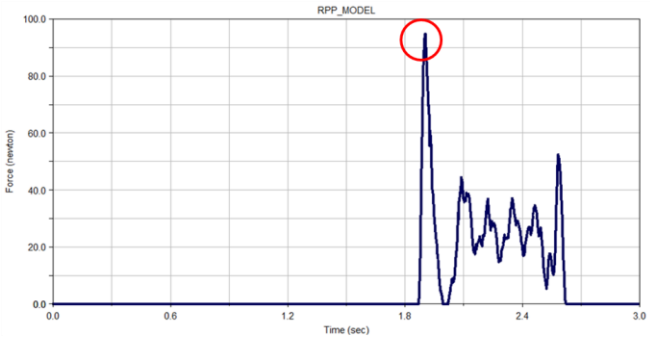


Fig.16. Time history of the track-ground contact force prior to geometry modification

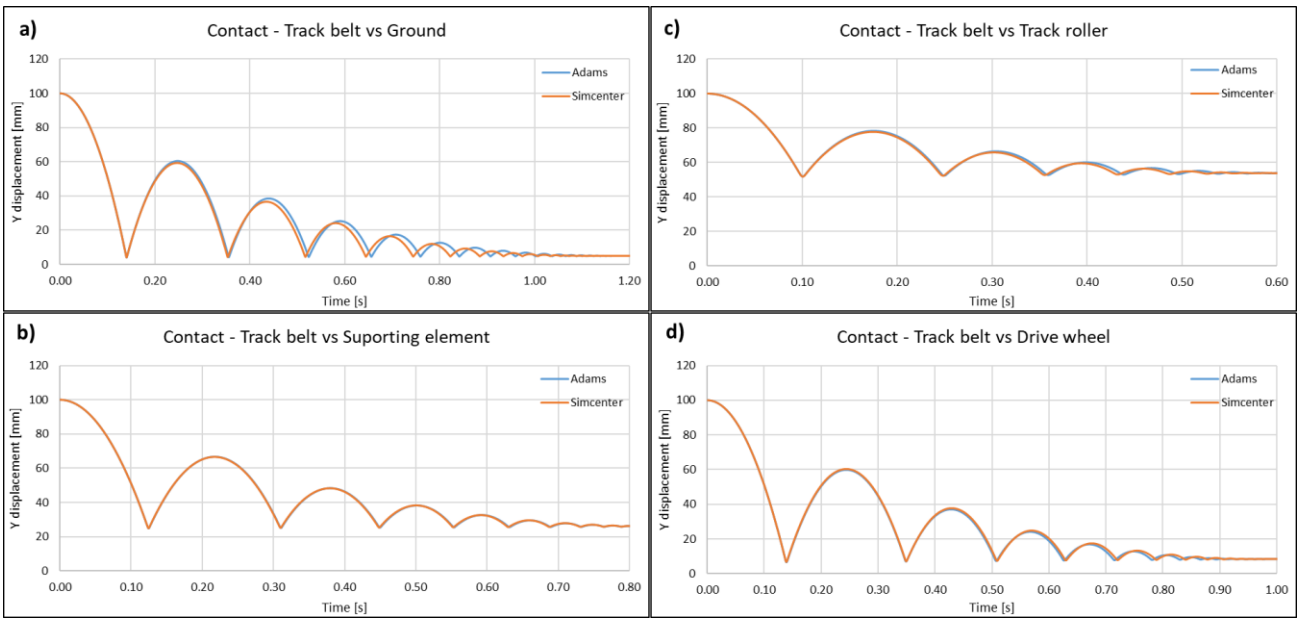


Fig.15. Graphical representation of the displacement of sphere 1 in the OY axis for different contact: a) track belt - ground, b) track belt - supporting element, c) track belt - track roller, d) track belt - drive wheel.

This article has been accepted for publication in a future issue of this journal, but has not been fully edited. Content may change prior to final publication.

Detailed investigation revealed that the primary cause of these anomalies was the interaction between sharp edges of the track grousers and the irregularities of the ground surface.
To eliminate the observed instabilities, the geometry of the track segments was simplified (Figure 17) by removing sharp edges while preserving the geometric interlocking between the track and the ground. After these modifications, the contact-force response became substantially more stable and the previously observed non-physical spikes were effectively eliminated (Figure 18).

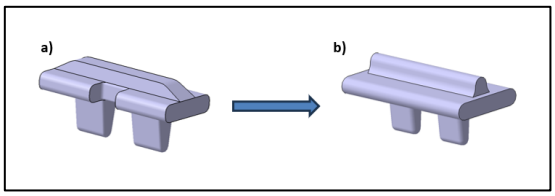


Fig.17. Track segment simplification: a) Track segment before modification, b) modified track segment

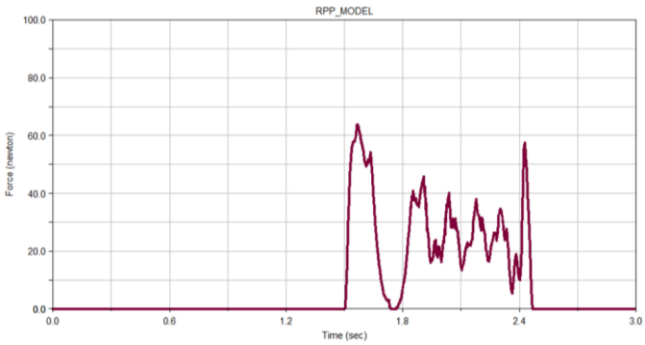


Fig.18. Time history of the track-ground contact force after geometry modification.

In subsequent iterations of the drivetrain model, additional modifications were introduced to improve the interaction between the drive wheel and the track segments. In the initial configuration, the contact was defined directly using CAD-based geometry (Figure 19), which resulted in undesirable phenomena such as excessive penetration and random force spikes. These effects were primarily caused by point contact between sharp edges and flat surfaces (Figure 20), leading to numerical instability of the model.

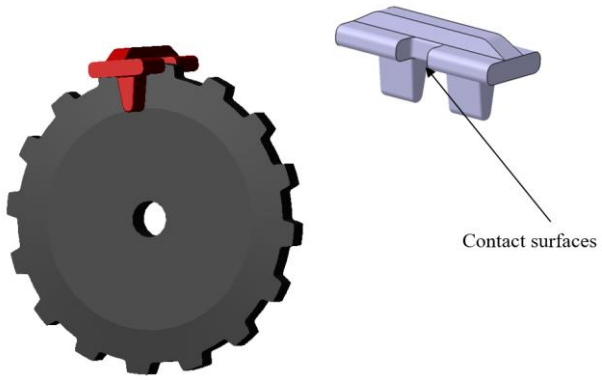


Fig. 19. Initial CAD-based contact between the drive wheel and track segment.

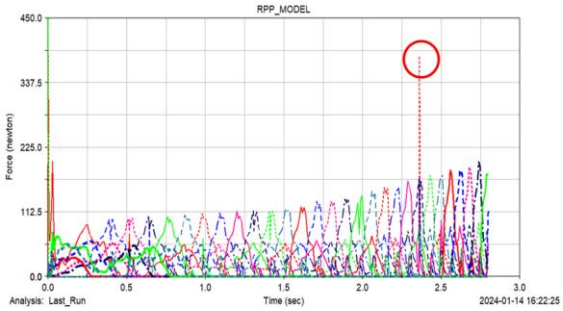


Fig. 20. Time history of the track-drive wheel contact force before geometry modification.

To eliminate the previously identified issues, a simplified sphere-plane contact model was introduced. A massless spherical element was placed at the centre of each track segment and acted as an intermediary for force transmission between the drive wheel and the track. Two independent contact formulations were assigned to this sphere: one representing the tangential (circumferential) force component and the other representing the radial (normal) force component acting perpendicular to the drive-wheel contact surface (Figure 21).

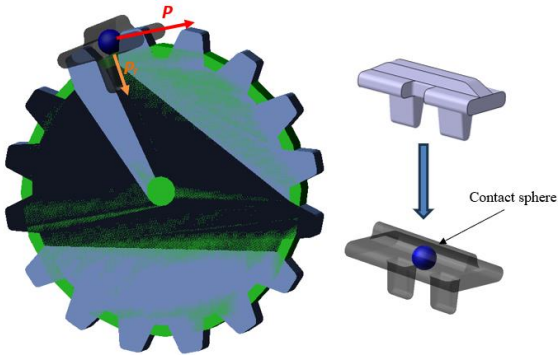


Fig. 21. Modified contact model between the drive wheel and track segment using a spherical interaction element.

The proposed modification substantially reduced non-physical force spikes, as confirmed by the contact-force time histories obtained for the updated configuration (Figure 22). The observed behaviour is also consistent with the theoretical interaction between a drive wheel and a track, according to which most of the transmitted torque is carried by a single tooth, while the remaining teeth contribute progressively less to load transfer.

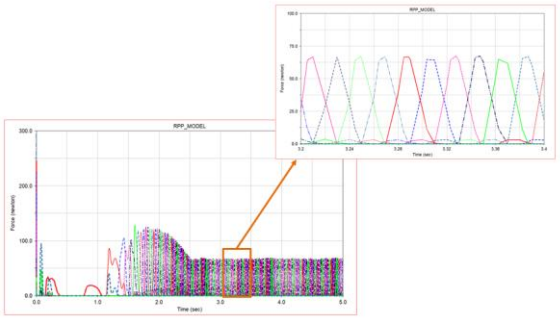


Fig. 22. Time history of the track- drive wheel contact force after contact model modification.

This article has been accepted for publication in a future issue of this journal, but has not been fully edited. Content may change prior to final publication.

The adopted contact modelling approach improved both numerical stability and physical consistency of the simulation results, which is essential for subsequent load analysis of the drivetrain system.

In the next stage, a time step sensitivity analysis was performed to evaluate the influence of integration step size on the simulation results. The objective was to determine an optimal time step ensuring a balance between numerical accuracy, model stability, and computational efficiency. Simulations with a total duration of 5 s were conducted, starting from a time step of 0.0001 s, which was subsequently increased by an order of magnitude in successive iterations.

The time-step sensitivity study was performed for straight-line motion of the UGV on a rigid flat surface. The vehicle motion was imposed by applying the same prescribed angular-velocity input to both drive wheels. Each simulation lasted 5 s, and the integration time step was varied from 0.0001 s to 0.1 s. The quantities used for comparison were the drive-wheel torque time history and the total computation time.

During the simulations, the driving torque at the drive wheel and the total computation time were evaluated for different time step values. The results are presented in Figure 23. The obtained results clearly indicate that decreasing the time step leads to a significant increase in computation time. For the smallest analysed time step (0.0001 s), the simulation time exceeded 100 minutes, whereas for the largest time step (0.1 s), it was reduced to less than 10 minutes.

At the same time, the time step has a pronounced effect on the predicted driving torque. For large time step values (0.1 s), the torque response exhibits significant oscillations and irregular behaviour, indicating insufficient numerical accuracy. As the time step decreases, the torque signal becomes progressively smoother and more stable. For time steps of 0.001 s and 0.0001 s, the differences between the results are minimal, suggesting convergence of the numerical solution.

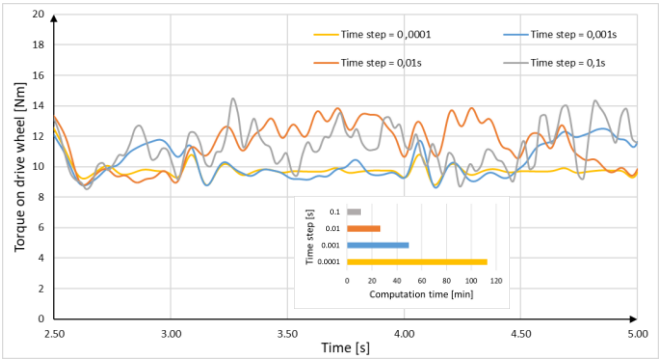


Fig. 23. Influence of integration time step on driving torque and computation time.

Based on the performed analysis, a time step of 0.001 s was selected as an optimal compromise between numerical accuracy and computational efficiency. Further reduction of the time step does not significantly improve the quality of the results while substantially increasing the computational cost.

The final stage of model verification involved assessing its sensitivity to vehicle speed during obstacle negotiation. A reference simulation scenario was defined as the traversal of a log obstacle, performed at three different velocities: 2, 4, and 6 km/h. A representation of the analysed case is shown in Figure 24, illustrating the model configuration before track-obstacle interaction as well as characteristic vehicle positions during the obstacle crossing process.

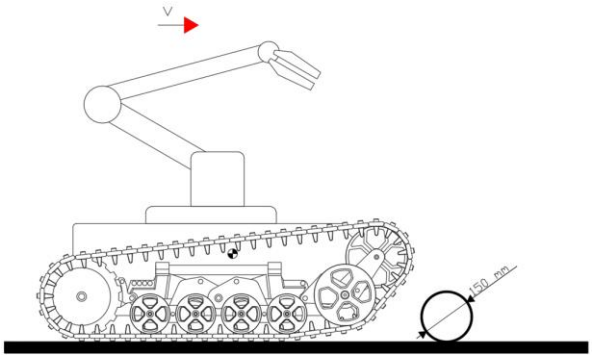


Fig. 24. Representation of the tracked vehicle crossing a log obstacle.

The simulation results are presented in Figure 25. Analysis of the obtained responses indicates a strong influence of vehicle speed on both the magnitude and character of the loads within the system. As the velocity increases, a clear rise in peak force values is observed in the drivetrain, track, and suspension components. The highest load levels occur at a velocity of 6 km/h, reflecting the increasingly dynamic nature of the interaction with the obstacle.

For the drive wheel, the reported load represents the equivalent circumferential force, calculated from the drive-wheel torque. Driving force represents the tangential force component responsible for torque transmission rather than the magnitude of the resultant contact force. An increase in its peak value is observed with increasing vehicle speed, with the highest values occurring during obstacle negotiation. A similar trend is evident in the track forces, where higher velocities lead to short duration but significantly higher force peaks, exceeding those observed at lower speeds.

The analysis of the Y-direction reaction force measured at the suspension-arm revolute joint reveals a change in the system behaviour. At lower speeds, the response is predominantly quasi-static, whereas at higher speeds, dynamic effects become dominant, resulting in rapid force variations and increased irregularity of the load signals.

The obtained results confirm that the model correctly captures the relationship between vehicle speed and load response, demonstrating sensitivity to changes in operating conditions. This indicates that the model is suitable for further dynamic analyses, including extreme load evaluation and fatigue assessment.

This article has been accepted for publication in a future issue of this journal, but has not been fully edited. Content may change prior to final publication.

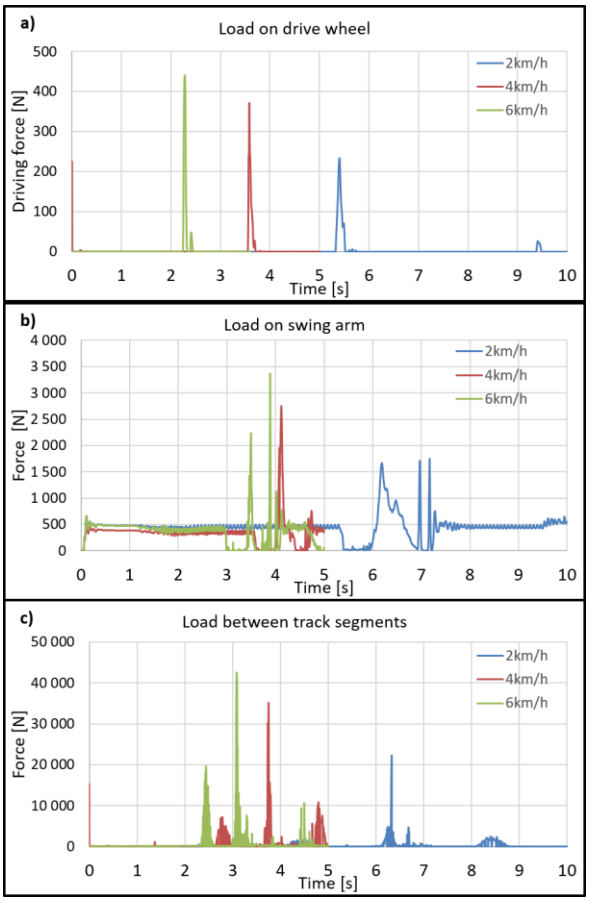


Fig. 25. Influence of vehicle speed on load response during obstacle crossing: a) load on drive wheel, b) load on swing arm, c) load between track segments.

4. CONCLUSIONS

The verification process focused on the parameterisation and assessment of key subsystems, including the track belt model, contact interactions, suspension elements, and numerical solver settings. The results of static and dynamic tests of the track model demonstrated a strong dependence of system response on stiffness and damping parameters, particularly in terms of deflection, oscillation amplitude, and stabilisation time. Different parameter configurations led to significant variations in dynamic behaviour, confirming high sensitivity of the track model to input parameters.

The calibration of contact interactions using a comparative approach with Simcenter simulations resulted in satisfactory agreement between the two numerical models, with an average relative error below 15%. This level of agreement was considered sufficient for the present numerical verification stage while maintaining simulation stability.

Additional verification stages included modification of contact geometry and formulation, which significantly reduced non-physical force oscillations and improved the consistency of simulation results. The introduction of simplified contact representations, such as the sphere-based interaction model, proved effective in stabilising force transmission between cooperating elements.

The influence of numerical parameters was also evaluated through time step sensitivity analysis. The results indicated convergence of the solution for smaller time steps, while a value of 0.001 s was identified as an optimal compromise between accuracy and computational efficiency.

Finally, the model was assessed under dynamic conditions during obstacle crossing. The results showed a clear increase in load magnitude and dynamic effects with increasing vehicle speed, confirming that the model correctly captures the relationship between operating conditions and system response. Overall, the performed numerical verification demonstrated that the developed model provides stable, repeatable, and physically consistent results within the analysed simulation conditions. The resulting parameter set provides a basis for subsequent experimental validation of the complete UGV model and, following validation, for detailed analyses of drivetrain and undercarriage loads.

FUNDING

This work was financed by the Military University of Technology under the research project UGB 22-104/2026 (531-000104-W100-22).

This article has been accepted for publication in a future issue of this journal, but has not been fully edited. Content may change prior to final publication.

REFERENCES

[1] I. Munasinghe and A. Perera, "A comprehensive review of UAV–UGV collaboration: Advancements and challenges," *J. Sens. Actuator Netw.*, vol. 13, p. 81, 2024, doi: 10.3390/jsan13060081.

[2] V. V. Vantsevich and M. V. Blundell, Eds., *Advanced Autonomous Vehicle Design for Severe Environments*. Amsterdam, The Netherlands: IOS Press, 2015.

[3] M. Kumar, N. Ramakrishna, and A. Kandagatla, "Design and fabrication of unmanned ground vehicle (UGV)," *Int. J. Eng. Manag. Res.*, vol. 5, pp. 239–245, 2015.

[4] A. Rubiec, K. Cieślik, P. Krogul, M. Łopatka, and M. Przybysz, "Evacuation of the injured using unmanned systems," *Probl. Mechatron. Armament Aviat. Saf. Eng.*, vol. 15, pp. 73–86, 2024, doi: 10.5604/01.3001.0054.7512.

[5] D. Bogale, Y. Nitta, and Y. Kuba, "Developing UGV for construction site," 2019.

[6] A. Bartnicki, J. Łopatka, T. Muszyński, and J. Wrona, "Concept of IED/EOD operations (CONOPs) for engineer mission support robot team," *J. KONES*, 2015. [Online]. Available: https://www.semanticscholar.org/paper/e0e553e71315580a4cde0d8aa0e32e5c5df2607e. [Accessed: 1 Dec. 2024].

[7] S. Konopka, P. Krogul, T. Muszyński, and M. J. Łopatka, "Mobility studies of an articulated unmanned platform with tracked running gear," *Logistyka*, vol. 4, 2014. [Online]. Available: https://repo.bg.wat.edu.pl/info/article/WAT7ea7676919624b169ca8a1fd374596ef. [Accessed: 1 Dec. 2024].

[8] M. Łopatka, "Heavy robots for C-IED operations," in *Challenges to National Defence in Contemporary Geopolitical Situation*, 2018, pp. 60–66, doi: 10.47459/cndcgs.2018.8.

[9] R. Bogue, "Detecting mines and IEDs: What are the prospects for robots?" *Ind. Robot*, vol. 38, pp. 456–460, 2011, doi: 10.1108/01439911111153992.

[10] A. Bartnicki, M. J. Łopatka, T. Muszyński, and A. Rubiec, "Hydropneumatic suspension of an engineering support robot," *Logistyka*, vol. 6, 2011.

[11] D. Topolsky *et al.*, "Development of a mobile robot for mine exploration," *Processes*, vol. 10, p. 865, 2022, doi: 10.3390/pr10050865.

[12] E. Colon, "An integrated robotic system for antipersonnel mines detection," *IFAC Proc. Vol.*, vol. 34, pp. 235–240, 2001, doi: 10.1016/S1474-6670(17)41711-3.

[13] T. Horváth, "Emergency cases at countering improvised explosive devices (C-IED) and their potential management," *Land Forces Acad. Rev.*, vol. 24, pp. 95–106, 2019, doi: 10.2478/raft-2019-0011.

[14] M. J. Łopatka and T. Muszyński, "Future robots using in C-IED detection," in *Challenges to National Defence in Contemporary Geopolitical Situation*, 2018, pp. 40–45, doi: 10.47459/cndcgs.2018.5.

[15] I. Bjelovuk and S. Pavlović, "Forensic examination of improvised explosive devices," *Bezbednost*, vol. 64, pp. 46–64, 2022, doi: 10.5937/bezbednost2203046B.

[16] T. Frey, "What is missing in offshore explosive ordnance disposal risk assessment?" *Toxics*, vol. 12, p. 468, 2024, doi: 10.3390/toxics12070468.

[17] R. Galvez and E. Dadios, "Threat object detection and analysis for explosive ordnance disposal robot," *Glob. J. Eng. Technol. Adv.*, vol. 11, pp. 78–87, 2022, doi: 10.30574/gjeta.2022.11.1.0074.

[18] A. Onțică and A. Gordeș, "The role of explosive ordnance disposal divers in eliminating the danger generated by naval mines," *Land Forces Acad. Rev.*, vol. 29, pp. 219–226, 2024, doi: 10.2478/raft-2024-0023.

[19] J. Carpenter, *The Quiet Professional: An Investigation of U.S. Military Explosive Ordnance Disposal Personnel Interactions with Everyday Field Robots*.

[20] A. Amin, "IED in Afghan war and in Pakistan's FATA war," 2021, doi: 10.13140/RG.2.2.33990.60484.

[21] J. Wrona, "Concept and development of engineer mission support robot," *J. KONES*, 2015. [Online]. Available: https://www.academia.edu/116686465. [Accessed: 1 Dec. 2024].

[22] M. Zarzycki, M. Dudek, A. Raźniak, A. Masłowski, A. Perski, and R. Czupryniak, "Development of criteria for the selection and investigation of PEMFC stacks as components of hybrid energy sources for UGVs," in *Proc. 28th Int. Conf. Methods Models Autom. Robot. (MMAR)*, 2024, pp. 568–573, doi: 10.1109/MMAR62187.2024.10680776.

[23] J. Y. Wong, *Theory of Ground Vehicles*, 3rd ed. New York, NY, USA: Wiley, 2001.

[24] J. Nawrocki, "Tracked running gear," *Szybkobieżne Pojazdy Gąsienicowe*, vol. 22, p. 1, 2007.

[25] D. Tomica, L. Śnieżek, and A. Rubiec, "Additive technologies in restoring the functionality of mobile robots," *Probl. Mechatron. Armament Aviat. Saf. Eng.*, vol. 15, pp. 31–46, 2024, doi: 10.5604/01.3001.0054.7505.

[26] J. Wang, K. Yang, B. Wu, and J. Wang, "Cooperative path planning for persistent surveillance in large-scale environment with UAV–UGV system," *IEEJ Trans. Electr. Electron. Eng.*, vol. 19, pp. 1987–2001, 2024, doi: 10.1002/tee.24157.

[27] B. Jin, Y. Sun, W. Wu, Q. Gao, and P. Si, "Deep reinforcement learning and ant colony optimization supporting multi-UGV path planning and task assignment in 3D environments," *IET Intell. Transp. Syst.*, vol. 18, pp. 1652–1664, 2024, doi: 10.1049/itr2.12535.

[28] Y. Shen and C. Wei, "Target tracking and enclosing via UAV/UGV cooperation using energy estimation pigeon-inspired optimization and switchable topology," *Aircr. Eng. Aerosp. Technol.*, vol. 95, 2022, doi: 10.1108/AEAT-05-2022-0143.

[29] M. Wei, S. Wang, J. Zheng, and D. Chen, "UGV navigation optimization aided by reinforcement learning-based path tracking," *IEEE Access*, vol. 6, pp. 1–1, 2018, doi: 10.1109/ACCESS.2018.2872751.

[30] M. József, "Concept of an UGV with Arduino device," *Hadmérnök*, vol. 9, pp. 140–148, 2014.

[31] I.-W. Park, T. Smith, H. Sanchez, S. W. Wong, P. Piacenza, and M. Ciocarlie, "Developing a 3-DOF compliant perching arm for a free-flying robot on the International Space Station," in *Proc. IEEE Int. Conf. Adv. Intell. Mechatron. (AIM)*, 2017, pp. 1135–1141, doi: 10.1109/AIM.2017.8014171.

[32] K. Panchal, C. Vyas, and D. Patel, "Developing the prototype of wall climbing robot," 2014.

[33] K. Majkut, "Inspection Robot Design for Liquid Storage Tanks," Ph.D. thesis, AGH University of Science and Technology, Kraków, Poland, 2015.

[34] A. Ugenti, R. Galati, G. Mantriota, and G. Reina, "Analysis of an all-terrain tracked robot with innovative suspension system," *Mech. Mach. Theory*, vol. 182, p. 105237, 2023, doi: 10.1016/j.mechmachtheory.2023.105237.

[35] F. Huzaefa and Y.-C. Liu, "Force distribution and estimation for cooperative transportation control on multiple unmanned ground vehicles," *IEEE Trans. Cybern.*, vol. 53, pp. 1335–1347, 2023, doi: 10.1109/TCYB.2021.3131483.

[36] A. Rubiec, A. Dąbrowska, and M. Łopatka, "Specificity of excitations acting on engineering support robot suspension systems," *Logistyka*, vol. 6, 2011. [Online]. Available: http://yadda.icm.edu.pl/baztech/element/bwmeta1.element.baztech-article-BPG8-0087-0016. [Accessed: 3 Dec. 2024].

[37] S. Jiang, W. Song, Z. Zhou, and S. Sun, "Stability analysis of the food delivery robot with suspension damping structure," *Heliyon*, vol. 8, p. e12127, 2022, doi: 10.1016/j.heliyon.2022.e12127.

[38] O. Alexa, T. Ciobotaru, L. Ș. Grigore, T. L. Grigorie, A. Ștefan, I. Oncioiu, I. Priescu, and C. Vlădescu, "A review of mathematical models used to estimate wheeled and tracked unmanned ground vehicle kinematics and dynamics," Mathematics, vol. 11, no. 17, Art. no. 3735, 2023, doi: 10.3390/math11173735.

[39] H. Skovbjerg, "Track models in ATV," 2024. [Online]. Available: https://www.mscsoftware.se/solutions/toolkits/atv/track_models.htm. [Accessed: 11 Apr. 2024].

[40] T. Nabagło, "Modeling and simulation of a tracked vehicle in MSC Adams," *Mechanika*, vol. 108, pp. 375–382, 2011.

[41] F. Mocera and A. Nicolini, "Multibody simulation of a small-size farming tracked vehicle," *Procedia Struct. Integr.*, vol. 8, pp. 118–125, 2018, doi: 10.1016/j.prostr.2017.12.013.

[42] D. Szpaczyńska, M. J. Łopatka, and P. Krogul, "The running gear construction impact on overcoming obstacles by light high-mobility tracked UGV," *J. Terramech.*, vol. 112, pp. 1–17, 2024, doi: 10.1016/j.jterra.2023.11.003.

[43] Grazioso, A., Ugenti, A., Galati, R., Mantriota, G., & Reina, G. (2023). Modelling and validation of a novel tracked robot via multibody dynamics. Robotica, 41(10), 3211– 3232. DOI: 10.1017/S0263574723000966.

[44] A. Febbraro, M. Dutto, L. Bascetta, and G. Ferretti, "Object-oriented modelling of a tracked vehicle for agricultural applications," Comput.

This article has been accepted for publication in a future issue of this journal, but has not been fully edited. Content may change prior to final publication.

Electron. Agric., vol. 230, Art. no. 109921, 2025, doi: 10.1016/j.compag.2025.109921.
[45] J. Matej, "Tracked mechanism simulation of mobile machine in MSC Adams/View," *Res. Agric. Eng.*, vol. 56, pp. 1–7, 2010, doi: 10.17221/9/2009-RAE.
[46] T. Nabaglo, J. Kowal, and A. Jurkiewicz, "Construction of a parametrized tracked vehicle model and its simulation in MSC Adams," *J. Low Freq. Noise Vib. Act. Control*, vol. 32, pp. 167–173, 2013, doi: 10.1260/0263-0923.32.1-2.167.
[47] D. Szpaczyńska, M. J. Łopatka, P. Krogul, et al., "Comparison of multi-tracked running gears in terms of obstacle negotiation capabilities," Appl. Sci., vol. 15, no. 4, p. 1696, 2025, doi: 10.3390/app15041696.
[48] PIAP, "Mobile Robots for Special Applications." [Online]. Available: https://www.piap.pl/produkt/roboty-mobilne-do-zastosowan-specjalnych/.
[49] D. Szpaczyńska, M. J. Łopatka, and P. Krogul, "Susceptibility modeling of a rubber track for lightweight mobile robots," *Appl. Sci.*, vol. 13, p. 10533, 2023, doi: 10.3390/app131810533.
[50] *Adams 2021.2—Adams View Function Builder User Guide*. Hexagon. [Online]. Available: https://nexus.hexagon.com/documentationcenter. [Accessed: 4 Dec. 2024].
[51] "Material datasheet." [Online]. Available: https://www.matweb.com/. [Accessed: 24 Apr. 2026].

This article has been accepted for publication in a future issue of this journal, but has not been fully edited. Content may change prior to final publication.